



Characterization of a sCMOS-based high-resolution imaging system

Alberto Mittone,^{a,*} Ilja Manakov,^{b,†} Ludovic Broche,^c Christophe Jarnias,^a Paola Coan^b and Alberto Bravin^a

^aEuropean Synchrotron Radiation Facility, 71 Avenue des Martyrs, Grenoble 38000, France, ^bLudwig Maximilian University, Am Coulombwall 1, D-85748 Munich, Germany, and ^cHedenstierna Laboratory, Department of Surgical Sciences, Uppsala University, Sweden. *Correspondence e-mail: alberto.mittone@esrf.fr

Received 10 May 2017

Accepted 23 August 2017

Edited by A. Momose, Tohoku University, Japan

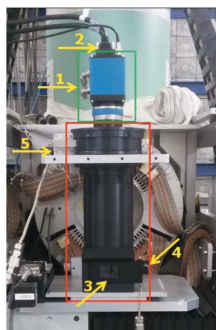
† These authors contributed equally to this work.

Keywords: image detector; X-ray imaging; image quality.

The detection system is a key part of any imaging station. Here the performance of the novel sCMOS-based detection system installed at the ID17 biomedical beamline of the European Synchrotron Radiation Facility and dedicated to high-resolution computed-tomography imaging is analysed. The system consists of an X-ray–visible-light converter, a visible-light optics and a PCO.Edge5.5 sCMOS detector. Measurements of the optical characteristics, the linearity of the system, the detection lag, the modulation transfer function, the normalized power spectrum, the detective quantum efficiency and the photon transfer curve are presented and discussed. The study was carried out at two different X-ray energies (35 and 50 keV) using both 2× and 1× optical magnification systems. The final pixel size resulted in 3.1 and 6.2 μm, respectively. The measured characteristic parameters of the PCO.Edge5.5 are in good agreement with the manufacturer specifications. Fast imaging can be achieved using this detection system, but at the price of unavoidable losses in terms of image quality. The way in which the X-ray beam inhomogeneity limited some of the performances of the system is also discussed.

1. Introduction

Complementary metal-oxide semiconductor (CMOS) detectors together with amorphous silicon and amorphous selenium flat-panels are today the main challengers to charge-coupled devices (CCDs), which have dominated scientific imaging applications (Gruner *et al.*, 2002) for years. Although all these sensors present specific features and have a broad range of applications, none can match so far the high image fidelity provided by CCD detectors in terms of readout noise, quantum efficiency and dynamic range. However, since in the CCD architecture each pixel is read sequentially, these detectors typically are characterized by slow readout speeds, resulting in few frames s⁻¹ (Gruner *et al.*, 2002). Many attempts have been made to address this issue, resulting in electron-multiplying CCDs (Denvir & Conroy, 2003) and interline CCDs (TD Luo *et al.*, 2016). Although these innovations lead to higher readout speeds, they cannot maintain the low level of noise. In 2009, the joint venture formed by Andor Technology, Fairchild Imaging and PCO AG released a new type of CMOS detector. This device was specifically developed for scientific imaging applications and was hence named scientific CMOS (sCMOS). The detailed specifications of this new device are reported in a white paper (http://ridl.cfd.rit.edu/products/sCMOS/scmos_white_paper_8mb.pdf): it is claimed that it would combine the best of CCD and CMOS sensors in one device, without compromising any of the imaging parameters.



Performing fast high-resolution image acquisitions is the new frontier of preclinical *in vivo* micro-computed tomography, which also requires that the radiation delivered is kept as low as possible. For this purpose, at the ID17 ESRF, the PCO.Edge5.5 has replaced the FReLoN camera in many imaging applications (Coan *et al.*, 2006), in particular because of the possibility of reaching higher frame rates. However, in order to be able to work efficiently with this new device, we performed a full characterization of the performance of the entire imaging system. In this paper we present the findings of our investigation where the PCO.Edge5.5 was coupled with $1\times/2\times$ optics systems and an yttrium aluminium garnet (YAG) scintillator of 350 μm thickness. The final pixel sizes using these configurations were 6.2 and 3.1 μm , respectively. The parameters investigated were the imaging system spatial distortions, its linearity, the detection lag effect, the modulation transfer function (MTF), the normalized noise power spectrum (NNPS), the quantum efficiency (QE) and the photon transfer curve (PTC).

2. Materials and methods

2.1. X-ray beam properties

We performed our measurements in the satellite building of the ID17 beamline of the ESRF, located at 145–155 m from the X-ray source. The ID17 source is a 21-pole, 150 mm-period, variable field wiggler ($B_{\text{max}} = 1.6\text{ T}$) of the ESRF 6.04 GeV electron storage ring. The photon source size is $125\ \mu\text{m} \times 25\ \mu\text{m}$ (H \times V), expressed as full width at half-maximum (FWHM), which produces a high intense continuous spectrum of X-rays up to several hundred keV. The maximum beam dimensions at the experimental station are $\sim 150\ \text{mm} \times 10\ \text{mm}$ (H \times V). The beam is monochromated by a fixed-exit Si(111) double bent Laue crystal; this device can deliver quasi-monochromatic X-ray beams ($\Delta E/E \simeq 10^{-4}$) in the energy range 25–150 keV (Suortti *et al.*, 2000). The beam is quasi-parallel with a divergence of $\leq 1\ \text{mrad}$ horizontally and $\ll 0.1\ \text{mrad}$ vertically. The monochromatic beam intensity can be controlled *via* a set of PMMA attenuators positioned just after the monochromator. The distance between the optical elements used in this work (*i.e.* pinhole and blades) and the detector was kept to the minimum allowed by the setup (about 50 cm) with the aim of minimizing penumbra effects.

2.2. The PCO.Edge5.5 camera

The PCO.Edge5.5 camera is manufactured and distributed by PCO AG. It features a 2560×2160 pixel sCMOS image sensor, which has total dimensions of $16.6\ \text{mm} \times 14\ \text{mm}$ and a pixel size of $6.5\ \mu\text{m} \times 6.5\ \mu\text{m}$. At full resolution, frame rates of up to $100\ \text{frames s}^{-1}$ can be achieved. This value can be increased further by vertically reducing the region of interest (ROI) of the acquired image. The device is equipped with Peltier cooling and is operated at a temperature of 5°C . There are three modalities for the readout of the sensor:

(i) In *rolling shutter* mode the exposure of the pixels starts and ends row by row. The exposure time is the same for all

pixels, but the start and end times differ. The exposure begins at the top and bottom lines first. The amount of simultaneously exposed lines is defined by the exposure time, which can be adjusted from 500 μs to 2 s. While this mode offers the highest frame rates, it can also lead to distortions when imaging fast-moving objects.

(ii) In *global shutter* mode the exposure starts and ends for all pixels simultaneously, but the achievable frame rate is cut in half since the image cache has to be emptied globally before each image acquisition. The possible exposure time ranges from 20 μs to 100 ms.

(iii) *Global reset* is a mixture of the two previous modes. Exposure starts for all pixels at the same time but they stay exposed until the readout, which is performed row by row starting from the top and bottom lines. Therefore, the closer the line is to the middle of the sensor, the longer it will be exposed. Exposure times from 20 μs to 2 s can be chosen in this mode.

For our measurements, the device was mostly operated in rolling shutter mode unless exposure times below 500 μs were required, in which case the camera global shutter was used.

2.3. Optics and scintillation screen

The optical system coupled to our sCMOS camera is composed of a $1\times/2\times$ system of lenses, allowing a final effective pixel size of 6.2 μm or 3.1 μm , according to the magnification used. The $1\times$ lens system presents a numerical aperture (NA) of 0.227 with a field of view (FOV) of $14.08\ \text{mm} \times 11.65\ \text{mm}$ while the $2\times$ optics has NA = 0.170 and FOV = $7.04\ \text{mm} \times 5.94\ \text{mm}$. Among the possible available choices, we used a YAG scintillator of thickness 350 μm for converting X-rays into visible light. This scintillator represents a good compromise between spatial resolution and detection efficiency. Its emission occurs at a wavelength of 535 nm, corresponding to green light, which matches well the peak QE of the sCMOS chip (Fig. 1). The properties of commonly used

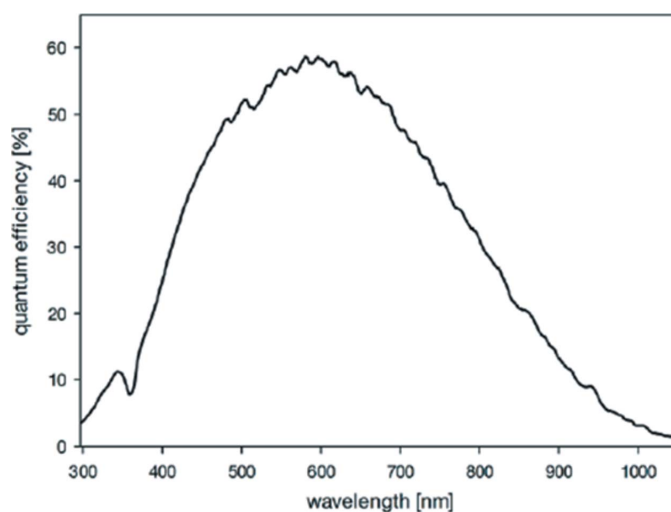


Figure 1
QE of the PCO.Edge5.5 sCMOS chip in terms of visible light (PCO.Edge5.5 datasheet, https://www.pco.de/fileadmin/user_upload/db/download/BR_pco_edge55_101.pdf).

Table 1
Scintillator properties as reported by Banhart (2008).

Scintillator	Peak emission (nm)	Decay time (ns) [†]	Density (g cm ⁻³)
Tb:Gd ₂ O ₂ S (Gadox)	630	1 × 10 ⁶ to 2 × 10 ⁶	7.32
Ce:LuAG	510	70	6.71
Ce:YAG	535	70	4.55
Ce:LYSO‡	420	40	7.15
BGO‡	480	300	7.13
Ce:LaBr ₃ ‡	375	30	5.08

[†] The decay time is defined by the time after which the intensity of the light pulse has returned to 1/e of its maximum value. [‡] These scintillator screens were not available during the experimental time.

scintillator screens are reported in Fig. 2 (absorption properties) and Table 1.

2.4. Distortions

Firstly, we verified that the lenses of both the optics systems do not cause any distortion to the acquired images. To this end, we used a pinhole with a diameter of 50 μm embedded in a tungsten block (UNT, Morbier, France). The pinhole was mounted on a motor stage and aligned with its surface parallel to the entrance screen of the detection system, as shown in Fig. 3. By using linear translation motors the pinhole was then displaced perpendicularly to the beam propagation, in both vertical and horizontal directions, in equidistant steps of 250 ± 2 μm on a well defined grid of points. At each step, the motor positions were recorded and an image of the pinhole was acquired. The motor positions were later correlated with the pinhole grid; data were analyzed using *ad hoc* Python code, and a map of recorded points *versus* the expected position was created.

2.5. Linearity

The linear response of the system has been verified over a range of different X-ray beam fluxes at a beam energy of

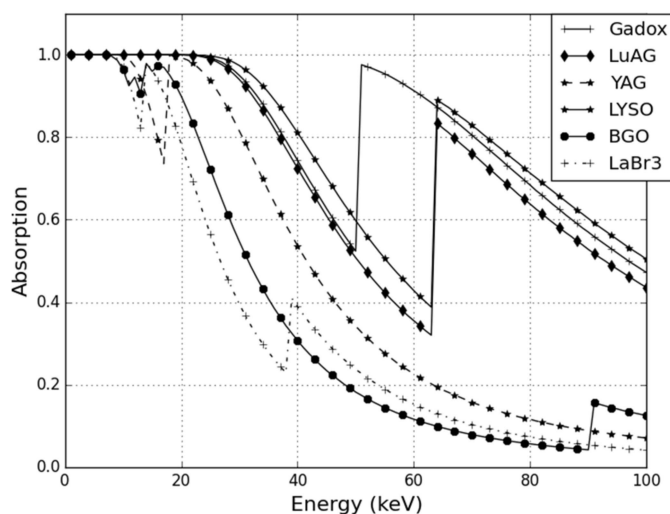


Figure 2
Absorption efficiency of different scintillator screens of 350 μm thickness. The curves have been calculated using the NIST database (<https://www.nist.gov/>).

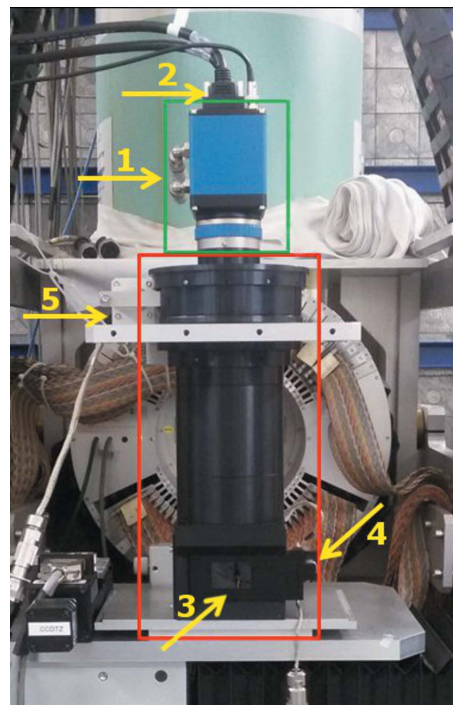


Figure 3
The water-cooled PCO.Edge5.5 camera mounted on the 2× optic system. The red rectangle indicates the scintillator-lenses system; the green rectangle indicates the PCO camera. (1) Connectors to the Peltier cooling system of the detector. (2) Camera link cables transferring the signal to the detector server. (3) Carbon window protecting the scintillator. (4) Motor used to adjust the focus of the system. (5) Motor used to align the lines of the PCO sensor with respect to the sample stage.

35 keV. This is an important step for the subsequent analysis of the detector in the spatial-frequency domain, since this study is based on the linear systems theory approach (Cunningham, 2000). System linearity is also necessary to directly use the pixel values in the following calculations, without the need of conversion. For this measurement, the beam flux impinging on the detector was varied using PMMA slabs of different thicknesses. For each plastic attenuator the photon flux was measured with a calibrated ionization chamber (PTW 31010 calibrated by PTB Freiburg, Germany) and several white-field images were recorded at each value of the absorber thickness. For each image the mean pixel value was calculated over the same central 512 × 512 and 2560 × 1000 pixel (H × V) ROIs and plotted against the number of incoming photons. The linearity of the system was then determined as the root mean square of the distances between the points and the linear regression line.

Because of the fixed emitted wavelength of the scintillator, measurements were performed at a single energy. The conversion ratio, at different energies and for different scintillator screens, can be calculated by considering the absorption properties of the scintillator (Fig. 2).

2.6. Detector lag

The collection of the accumulated charges in the device does not happen instantaneously. This can give rise to so-

called lag effects, where charges collected in a previous acquisition influence the next acquisition, if the time between images is too short. This effect might be of particular importance in fast imaging. In general, there are two types of lag effects: additive and multiplicative. Additive lag arises when charges generated during a previous exposure of the detector are still present on the chip at the time of the next acquisition and hence increase the count values on the next image. Multiplicative effects occur when the exposure of the detector changes the amplifier gain of the individual pixels. In order to measure the detector lag, we used a test that is detailed in the International Electrotechnical Commission 2003 (IEC, 2003) standard guidelines. We used a 3 mm-thick tungsten blade as a high-contrast object and compared areas of subsequent images that were exposed to the beam (ROI1) or obscured by the blade (ROI2). The tungsten blade was the same as that employed in the MTF measurement. Its thickness was chosen to completely shield the beam up to 50 keV, which is the highest energy used in the measurements. For the evaluation of the additive effect, an image of the blade, f_1 , was taken, followed by the acquisition of a dark-field image (*i.e.* camera not exposed to X-rays), f_2 . In our measurements, a series of dark fields, $f_2(t)$, acquired at different times after the exposure, was taken in order to evaluate the temporal evolution of the lag as well. The criterion for passing this test (*i.e.* negligible additive lag effects) is

$$\frac{f_{1\text{ROI2}} - f_{2\text{ROI1}}}{f_{1\text{ROI1}}} \leq 0.005. \quad (1)$$

To evaluate the multiplicative effects, we also acquired a series of images. The camera was exposed while the tungsten blade was vertically moving through the beam at a high speed of 100 mm s^{-1} . The blade was aligned in such a way that only half of the field of view was covered during the motion. To evaluate the effect of multiplicative lag we considered the images acquired at different times: first a white-field image, f_1 , then an image of the blade (not used), and lastly a white-field image again, f_2 . For this test the null criterion (*i.e.* negligible multiplicative lag effects) is

$$\frac{(f_{1\text{ROI2}} - f_{1\text{ROI1}}) - (f_{2\text{ROI2}} - f_{2\text{ROI1}})}{\frac{1}{2}(f_{1\text{ROI1}} + f_{2\text{ROI1}})} \leq 0.005, \quad (2)$$

with $f_{X\text{ROI}Y}$ ($X = 1, 2$ and $Y = 1, 2$) being average pixel values in a 700×700 pixel ROI. The null criterion test was calculated by considering $f_2(t)$, with t corresponding to different frames in order to evaluate its temporal evolution.

The aim was to find the minimum time interval between exposures/image acquisitions, so that both criteria are met simultaneously.

2.7. Modulation transfer function

The MTF is a universally accepted measure of the spatial resolution of a linear imaging system. It is defined as the amplitude of the two-dimensional Fourier transform of the system response to a delta-peak input signal, the so-called point spread function (PSF) (Cunningham, 2000). Analogously,

a one-dimensional MTF can be calculated from a line spread function (LSF), which is the system response to a line of delta-peak input signals. In practice, it is more common to opt for the second method, since it is technically challenging to generate a single delta-peak input signal. We measured the MTF following the edge technique (Fujita *et al.*, 1992), which was applied using the tungsten blade described in the previous paragraph. Imaging this edge yields to the edge spread function (ESF), which is the system response to a step-like signal. The LSF can then be calculated from the ESF by performing discrete differentiation; however, this procedure can drastically increase the noise present in the data. For this reason, we decided to use an alternative approach proposed by Boone & Seibert (1994), which consists of using an analytical model to fit the ESF from which the LSF can be calculated. By Fourier transforming the LSF and taking the absolute value, we obtained the one-dimensional MTF (Cunningham, 2000). To reduce or overcome the aliasing, the blade was placed in front of the detector window at a slight angle ($\sim 0.2^\circ$) with respect to the detector pixel lines (Dobbins, 2000). This method has the benefit of increasing the sampling rate of the ESF which allows for the calculation of the pre-sampling MTF (that is aliasing-free). The MTFs presented in this paper are the averages of a number of individual MTFs (64 in the vertical and 74 in the horizontal direction) from different parts of the detector. These individual MTFs were obtained by aligning the edge horizontally (vertically) at the left side (top) of the detector and shifting the edge in equidistant steps of $250 \mu\text{m}$ to the right side (bottom) after each image acquisition. For an easier comparison, the MTFs have been normalized to their value at zero frequency (MTF[0]) after averaging. Measurements were performed at photon energies of 35 keV and 50 keV for both the $1\times$ and $2\times$ lens systems. Particular attention was paid in the alignment of the blade to avoid penumbra effects due to its relatively large thickness (*i.e.* the blade cross section has to be perfectly perpendicular to the detector).

2.8. (Normalized) noise power spectrum

The noise power spectrum (NPS) is a characterization of the imaging system noise in the spatial frequency domain. It incorporates all noise sources present in the imaging process, which includes the quantum noise of the X-ray beam, as well as the noise introduced by the optical elements along the X-ray path, the detector scintillation screen and the electronics. The NPS decomposes the noise in spatial frequencies making it a useful method for quantifying not only the amount but also the nature of the noise. The two-dimensional digital NPS is calculated as (Cunningham, 2000)

$$\text{NPS}(u_i, v_j) = \frac{\Delta x \Delta y}{N_x N_y} \left\langle | \text{DFT2}(n_{ij}) |^2 \right\rangle, \quad (3)$$

with Δx and Δy being the pixel size, N_x and N_y the horizontal and vertical image dimensions and n_{ij} the two-dimensional noise image. DFT2 denotes the discrete two-dimensional Fourier transform.

The NPS was measured as specified in the literature (IEC, 2003), *i.e.* as an average of Fourier transforms of half-overlapping 256×256 pixel sub-regions of white-field images at three different exposure levels.

We performed additional measurements of the NPS, employing only the sCMOS camera without the magnification and scintillator system, by using a 588 nm LED source (Kingbright Electronic Co) coupled with an integrating sphere (X-RITE LABSPHERE IAS-100-SF). The purpose of these measurements was to evaluate the effect of the artefacts due to the spatial inhomogeneity of the X-ray beam and the YAG scintillation screen.

The NPS from each subset was normalized with the square of the average signal \bar{d} in the subset to obtain the normalized noise-power spectrum (NNPS),

$$\text{NNPS}(u, v) = \frac{\text{NPS}(u, v)}{\bar{d}^2}. \quad (4)$$

This procedure further helps to suppress variations in beam intensity and makes comparison with the NNPS easier. The ensembles in the calculation of each NNPS consist of an NNPS of approximately 1700 subsets.

The NNPS for each axis was obtained by synthesis (Siewerdsen *et al.*, 2002; IEC, 2003). This means that seven NNPS from the rows/columns to either side of the central axis (while omitting the axis itself) were averaged. This method was applied to avoid the large uncertainty that the NPS typically exhibits at zero frequencies.

2.9. Detective quantum efficiency

As shown in the previous two paragraphs, MTF and NPS are effective tools for describing a system spatial resolution and noise properties, respectively. While these quantities are, on their own, meaningful, they do not allow a direct comparison of the performance of different devices. To this purpose, the MTF and the NNPS are combined in a single absolute quantity called detective quantum efficiency (DQE), which is defined as

$$\text{DQE}(u) = \frac{1}{\bar{q}} \frac{\text{MTF}(u)^2}{\text{NNPS}(u)}. \quad (5)$$

Here, \bar{q} is the average number of incoming quanta per unit area. The DQE is an easily comparable quantity among different detectors as it gives the fraction of photons that an ideal detector (*i.e.* one that does not increase noise or degrade spatial resolution) would need to produce the same signal-to-noise ratio.

2.10. Photon transfer curve

The final measurement we performed on the PCO.Edge 5.5 deals with a method devised by J. R. Janesick (Janesick *et al.*, 1985; Janesick, 2007), called the photon transfer curve (PTC). A PTC is obtained by first recording a series of images at increasing integration times over the full dynamic range of the detector from which noise is calculated (as root mean square)

and then plotted against the average signal for each image on a logarithmic scale.

The underlying theory is that the noise in the images σ_{total} is composed of three components: σ_{read} represents the noise from the readout mechanism; $\sqrt{q/k}$ is the shot noise inherent to the photon nature of light, where q is the signal in analog-to-digital units (ADU) and k is the conversion gain in electrons per ADU; $\text{FPN} \times q$ is the fixed pattern noise due to the difference in sensitivity of the individual pixels. This results in (Lytaev *et al.*, 2014)

$$\sigma_{\text{total}} = \left[\sigma_{\text{read}}^2 + \left(\sqrt{q/k} \right)^2 + (\text{FPN} \times q)^2 \right]^{1/2}. \quad (6)$$

By assuming ergodicity (*i.e.* a system that presents the same behaviour averaged over time as averaged over space, in its phase space, of all the states of the system), we decided to generate a PTC for each individual pixel rather than for a region of interest. To this aim, we acquired sets of 30 white-field images at 198 different integration times in the range [0.5, 2000] ms and sets of 30 dark-field images at 20 different integration times in the same time range. For the white-field images the detector was illuminated with the LED and integrating sphere described in §2.2. From each set the root mean square and average count for each pixel were calculated. The obtained pixel-wise PTCs were successively used to generate a gain map, a readout noise map and a full-well map of the detector.

3. Results and discussion

3.1. Linearity

Fig. 4 reports the result of the linearity measurements. Both the average number of incoming photons and the average number of counts in the image have been normalized to the

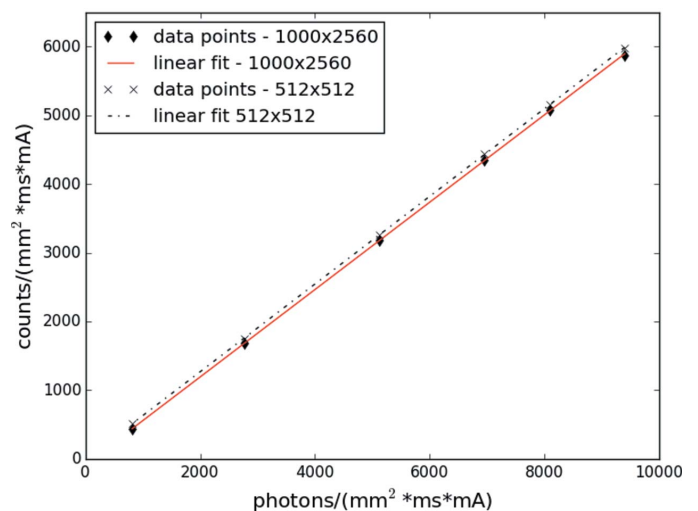


Figure 4 Plot of average incident photons *versus* average detector counts at 35 keV. Both were normalized to the unit area, time and synchrotron storage ring current. The value of the slope is 0.636, with an intercept of 0.13 for the 1000×2560 ROI and of 0.639 with an intercept of 0.05 for the 512×512 ROI.

unit area (expressed in mm^2), the time (ms) and the electron current in the storage ring of the synchrotron source (mA). The detector exhibits a negligible non-linearity: the root-mean-square error of the data points to a linear fit was found to be less than 0.1%.

The conversion factor from photons to digital counts computed from the average of the slopes of the fits in Fig. 4 was found to be 63.7%. This value is extremely close to the 65.0% that we calculated from the thickness and absorption coefficient of the YAG scintillator and the vendor's specifications for the QE and gain ($0.46 \text{ electrons count}^{-1}$) of the PCO.Edge. The QE was given by the PCO in the form of a peak value of 60% at a wavelength of 600 nm. The YAG scintillator emits light at 550 nm. The QE of the detector should be slightly lower at this wavelength, which may explain the small discrepancy between the calculation and the measurement.

3.2. Distortion

No evident distortions were detected meaning that the optical elements of the imaging system and setup do not introduce geometrical deformations of the signal (results not reported).

3.3. Lag tests

Fig. 5 reports the results of the detector lag tests. Being the response independent of the beam energy, the measurements were performed only at 35 keV. For the additive test we acquired a sequence of 50 images, with only the first one illuminated by X-rays and all the other ones of dark noise as explained in §2.6; the time between two consecutive frames was 200 ms. For the multiplicative test we acquired a sequence of 100 images during the movement of the blade through the detector FOV; the time interval between two images was 31 ms. To perform the test described at §2.6, we used the first image, then skipped the following ten images including the moving blade, and then used the other 89 consecutive white

fields. The times between two images were determined for the first test by the necessity of achieving good statistics for the evaluation of the lag criteria and for the multiplicative one by the maximum speed limit of the motor used to displace the blade through the beam. However, it is important to notice that the used time intervals between two images correspond to the typical ones used at ID17 in imaging experiments with the $3.1 \mu\text{m}$ optics.

The results of the tests are reported in Fig. 5, restricted to the most significant part of the trends (2 s and 1.8 s for the additive and multiplicative lags, respectively). The results show that the effects of both additive and multiplicative lag are negligible (values < 0.005). By following the trend of the additive test we can extrapolate that, for shorter acquisitions times ($< 100 \text{ ms}$ per projection), images may instead be affected by a residual signal, leading to a degradation of the overall spatial resolution. The effect would be small anyway compared with the natural blurring due to the movement of the sample in the case of fast tomography experiments. For example, if a continuous sample rotation of 18° s^{-1} is used to acquire 1000 angular projections over 180° , and the rotation axis, assumed to be vertical, lies in the center of the detector frame (corresponding to the pixel column 1280 in our case), each projection corresponds to the integral signal over about 0.14° . This would determine the mix up of the signal of ~ 3 pixels at the outer parts of the detector field of view.

3.4. Modulation transfer function

The averaged MTFs of the full imaging system and their relative standard deviation (STD), for the different combinations of optics and X-ray energies, are presented in Figs. 6 and 7 and Tables 2–5; the numerical values of the MTF at 50%, 10% and 5% are reported therein. The MTF curves fall short of the theoretical maximum given by the effective pixel size [*i.e.* $1/(2 \times \text{pixel size})$], which is $76.9 \text{ line pairs per millimetre}$ (lp mm^{-1}) for the $1\times$ and 153.8 lp mm^{-1} for the $2\times$ system. These discrepancies are probably due to scattering of visible

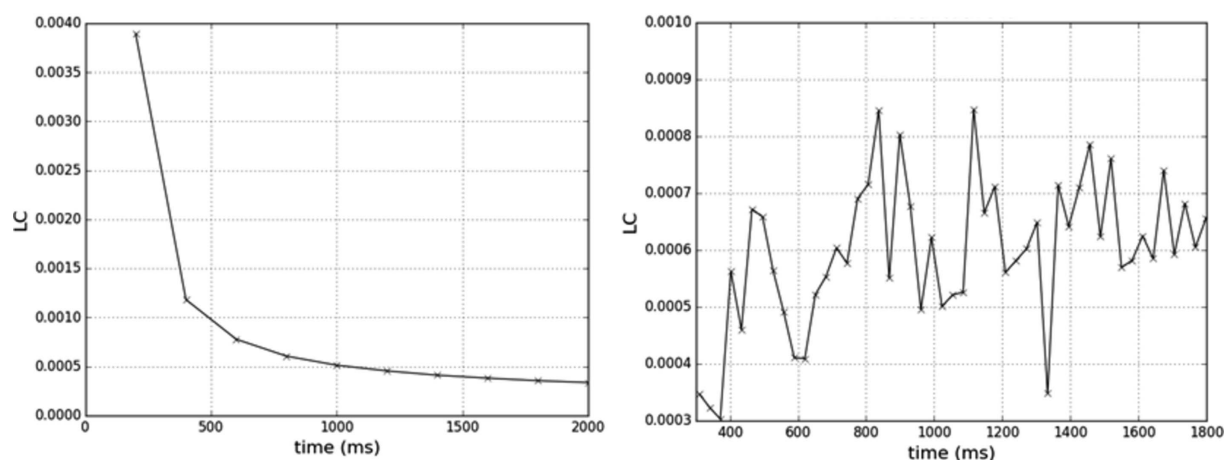


Figure 5 Left: calculated lag criteria (LC) versus time. Right: multiplicative lag effect. The fluctuations and the slightly growing trend are determined by the statistical noise and by the beam instabilities. Both criteria are passed because values are smaller than 0.005 (see §2.6).

Table 2
MTF values for the 2× optics case at 35 keV.

Each value presents a standard deviation < 0.1 lp mm⁻¹.

MTF value	Horizontal (lp mm ⁻¹)	Vertical (lp mm ⁻¹)
50%	44.4	40.4
10%	82.4	75.3
5%	94.7	86.7

Table 3
MTF values for the 2× optics case at 50 keV.

Each value presents a standard deviation < 0.1 lp mm⁻¹.

MTF value	Horizontal (lp mm ⁻¹)	Vertical (lp mm ⁻¹)
50%	43.5	41.1
10%	79.8	75.9
5%	91.3	87.1

Table 4
MTF values for the 1× optics case at 35 keV.

Each value presents a standard deviation < 0.1 lp mm⁻¹.

MTF value	Horizontal (lp mm ⁻¹)	Vertical (lp mm ⁻¹)
50%	23.7	23.7
10%	43.7	44.1
5%	50.1	50.6

Table 5
MTF values for the 1× optics case at 50 keV.

Each value presents a standard deviation < 0.1 lp mm⁻¹.

MTF value	Horizontal (lp mm ⁻¹)	Vertical (lp mm ⁻¹)
50%	23.2	25.5
10%	42.7	45.4
5%	49.0	52.2

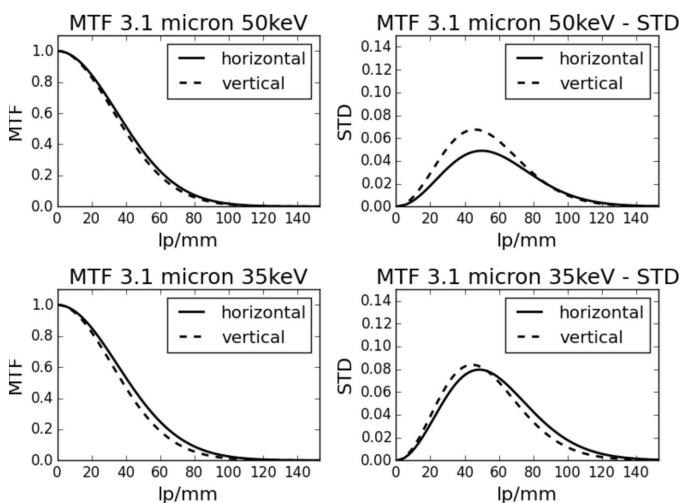


Figure 6
MTF graphs for the 2× optics case at 50 keV and 35 keV.

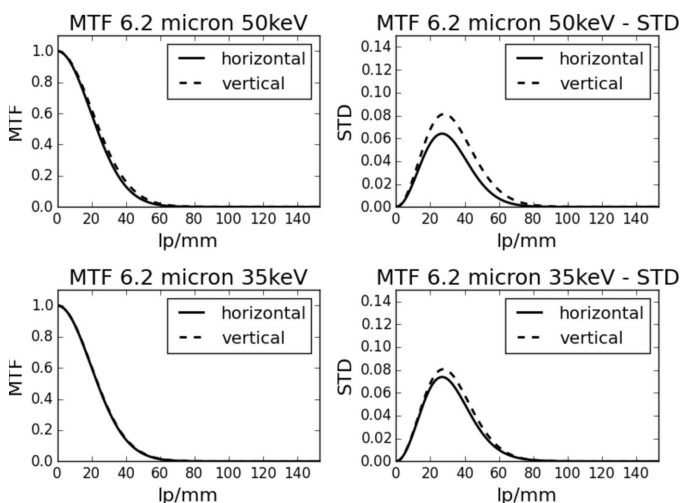


Figure 7
MTF graphs for the 1× optics case at 50 keV and 35 keV.

light in the scintillator screen, also depending on its thickness, which then broadens the PSF of the imaging system. One can see that the spatial frequencies corresponding to the first MTF zero almost double when using the 1× optics or 2× optics, as expected. The fact that the frequencies are not exactly doubled means that either the scintillator screen and/or the lens system act as a bottleneck for the spatial resolution. Our interpretation of the result is that there might have been a slight defocusing of the system (incorrect fluorescent-screen lenses distance) when we used the 2× optics and the presence of non-zero distance between the blade and the scintillation screen. Another observation is that there is a slight discrepancy between the vertical and horizontal MTF curves and values. The difference is more pronounced for the 2× optics.

The differences in performances obtained horizontally and vertically are to be attributed to the different value of divergence of our beam along the two directions associated with a non-zero distance between the blades and the detection system. We observe apparent superior performances for the vertical MTF due to a smaller beam divergence.

3.5. Normalized noise power spectrum

The NNPS for the system for both X-ray energies and both detector optics are presented in Figs. 8–11. Each plot shows both the vertical and horizontal NNPS side by side for the same setup.

The non-uniformities present in the beam profiles are typically correlated over relatively long distances and therefore they cause an increase in the low-frequency part of the NPS. To alleviate this effect, different de-trending methods have been applied on the data (Zhou *et al.*, 2011); however, among the various available methods we have chosen the subtraction method because of its capacity to correct for the beam inhomogeneity (mainly scintillator defects) represented by the bulk visible in the profile of the NNPS at low spatial frequencies (<5 lp mm⁻¹). The choice was driven and validated also by the results obtained using the LED source (data

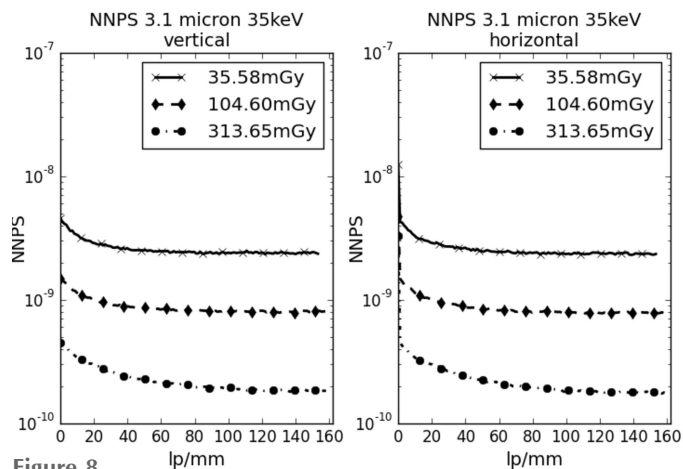


Figure 8
NNPS after the application of subtraction de-trending for the 2× optics case at 35 keV.

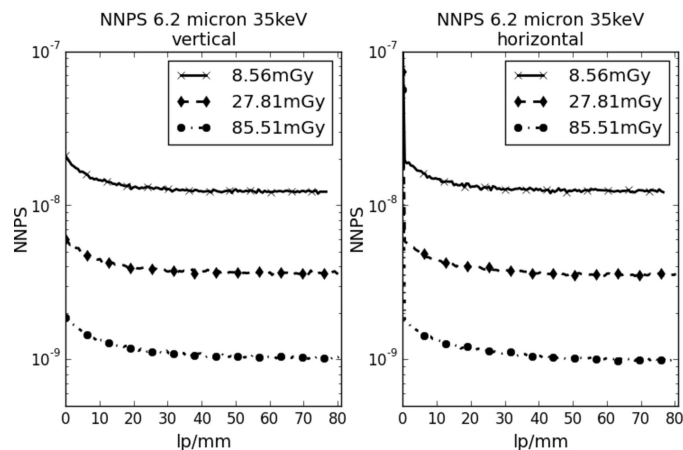


Figure 10
NNPS after the application of subtraction de-trending for the 1× optics case at 35 keV.

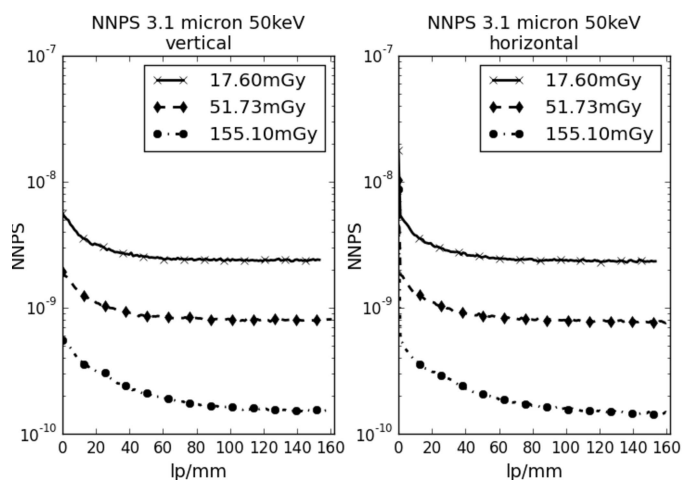


Figure 9
NNPS after the application of subtraction de-trending for the 2× optics case at 50 keV.

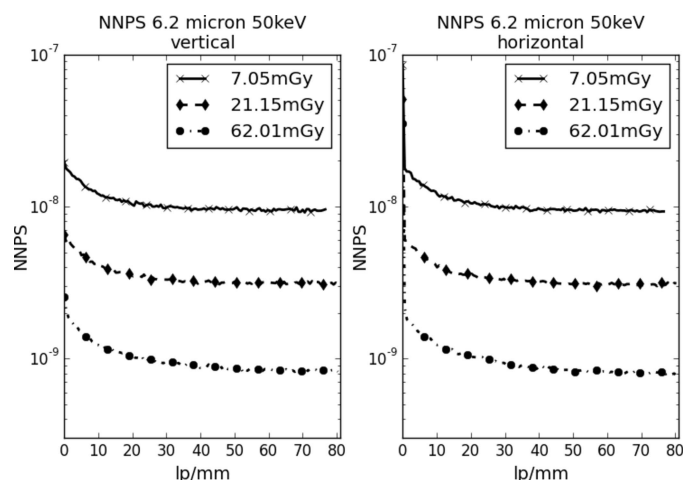


Figure 11
NNPS after the application of subtraction de-trending for the 1× optics case at 50 keV.

not reported), which did not suffer from the X-ray beam inhomogeneity. A drawback of the subtraction method is that it removes fixed pattern noise (differences in pixel sensitivity and amplification gain and small variations in the beam intensity due to defects in the different optical elements), which increases linearly with exposure; therefore, the curve exhibits a lower noise floor.

After the campaign of measurements presented in this work, we further investigated the origin of the scintillator defects. We found that these defects appear after a variable time of data acquisition (hours to days). They are related to the reversible formation of irregularities on the surface of the scintillator screen. We tested a new scintillator screen with the same physical characteristics (material, thickness) coated with a 15 nm-thick carbon layer on the X-ray entrance side. Repeated measurements proved that the coating prevents the formation of hotspots, with a consequent improvement of the imaging performances. Figs. 8–11 show plots of NNPS at three different levels of X-ray exposure expressed as dose in air. As

expected, following the natural Poisson distribution of the quantum noise, the NNPS is exposure-dependent, and presents higher values at lower exposures. The higher values around zero are given by the prevalence of the deterministic noise component. Stochastic contributions instead mask the low-frequency effects.

3.6. Detective quantum efficiency

The DQE evaluation has been made by considering the subtraction de-trending method, as explained above. Results are reported in Figs. 12 and 13. The shape of the DQE in the vicinity of zero is affected by the high contribution of the deterministic component of the NNPS. Higher values of DQE could be obtained by coupling the system with a more efficient scintillator screen (see Table 2). Normally it is expected that the DQE decreases with increasing exposure; this behaviour stems from the linear dependence of the fixed pattern noise on exposure and agrees with expectations. In our case the fixed

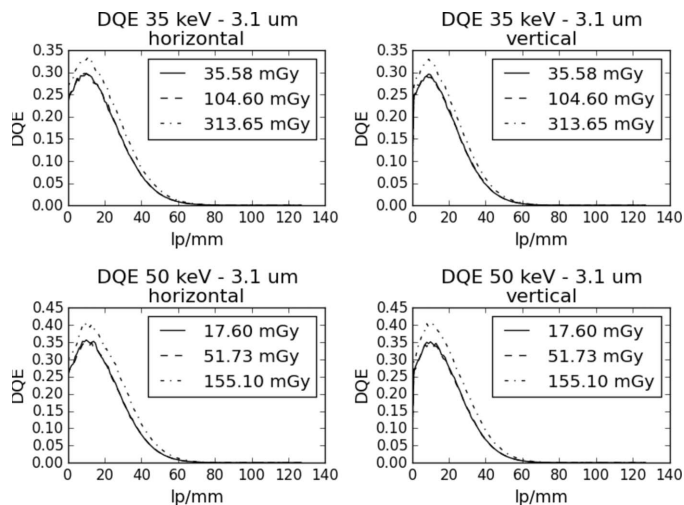


Figure 12
DQE with subtraction de-trending for the 2× optics case at 35 keV and 50 keV and for different exposure values.

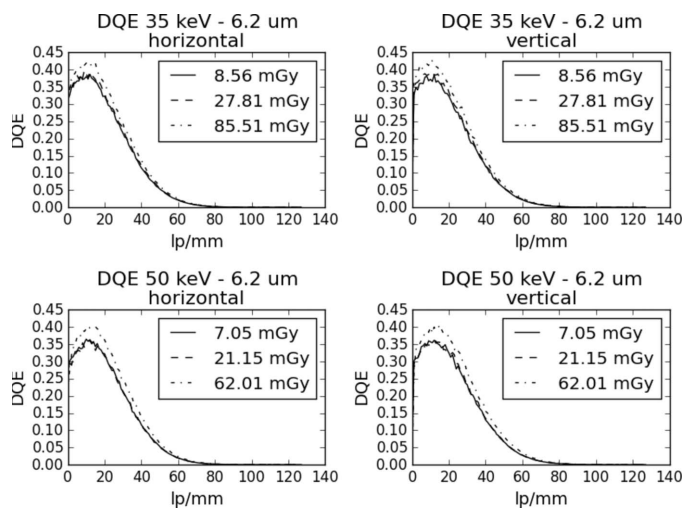


Figure 13
DQE with subtraction de-trending for the 1× optics case at 35 keV and 50 keV and for different exposure values.

pattern noise was removed by de-trending, so the sources of noise are the shot noise and the readout noise. The DQEs at the highest value of exposure present a similar shape but slightly higher values, but remain similar for the two lower levels of exposure. This behaviour is explained by a more pronounced effect of the readout noise at lower levels of exposure (Escartin *et al.*, 2016).

3.7. Photon transfer curve

The calculated PTC is reported in Fig. 14. The readout noise does not depend on the number of incoming photons q and therefore its contribution to the PTC is a constant. This is represented by the horizontal line in the first region (left side of Fig. 14) of the plot with zero signal. The shot noise is known from the statistical properties of photons and its expected value is the square root of the incoming number of photons divided by $\sqrt{q/k}$, which is the conversion factor of the system.

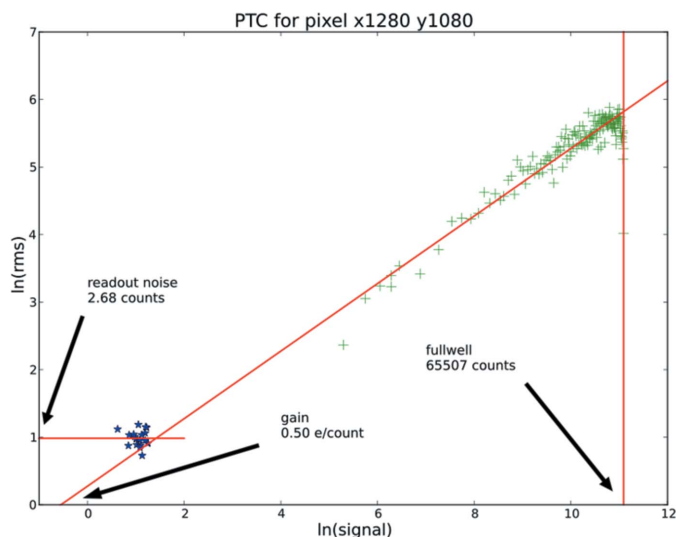


Figure 14
PTC for the single pixel (1280, 1080). White-field data are represented by green crosses and dark-field data by blue stars. The parameters readout noise, gain and full-well capacity for this particular pixel are reported in the figure.

This type of noise is reported in the second region of the graph. The line has a slope of 0.5 on a logarithmic scale. Once the fixed pattern noise becomes the dominant source of noise, the slope changes to 1 because the fixed pattern noise grows linearly with exposure time. This third region, which is characterized by a slope of 1, is not visible in the plot of Fig. 14 because it represents the PTC of a single pixel. When the integration time becomes so long that the maximum charge capacity of the imager pixels is reached, the noise drops down sharply as all of the pixels contain the same amount of counts. This point is referred to as the full-well capacity.

In Fig. 15(a) a map of the gain of the detector in electrons per count ($e^- \text{ count}^{-1}$) is reported. Generally the gain of the pixels matches the vendor’s specification of $0.46 e^- \text{ count}^{-1}$, although the average is slightly higher, *i.e.* $0.473 e^- \text{ count}^{-1}$. The gain seems to be higher in the central regions of the sensor than it is towards the left and right edges. A top half and a bottom half of the gain map can be distinguished and a structure of vertical lines is also visible. This reflects the architecture of the sCMOS sensor with a top and bottom readout and amplifiers for each column of pixels in each half. Overall the gain of the detector is fairly uniform with a standard deviation of 0.048%. The vendor’s claim of a non-uniformity of the photo-response of less than 0.05% is thus confirmed.

In Fig. 15(b) a map of the readout noise of the individual pixels in digital counts is reported. A close inspection of the map reveals a horizontal line with slightly increased readout noise in the center of the top and bottom halves of the sensor, respectively. In addition, the areas to the far right and far left sides seem to exhibit a slightly lower readout noise. However, these differences are negligible. Apart from this, no clear trends could be found in the image. Overall, the readout noise of the detector is exceptionally low, averaging at 3.03 digital

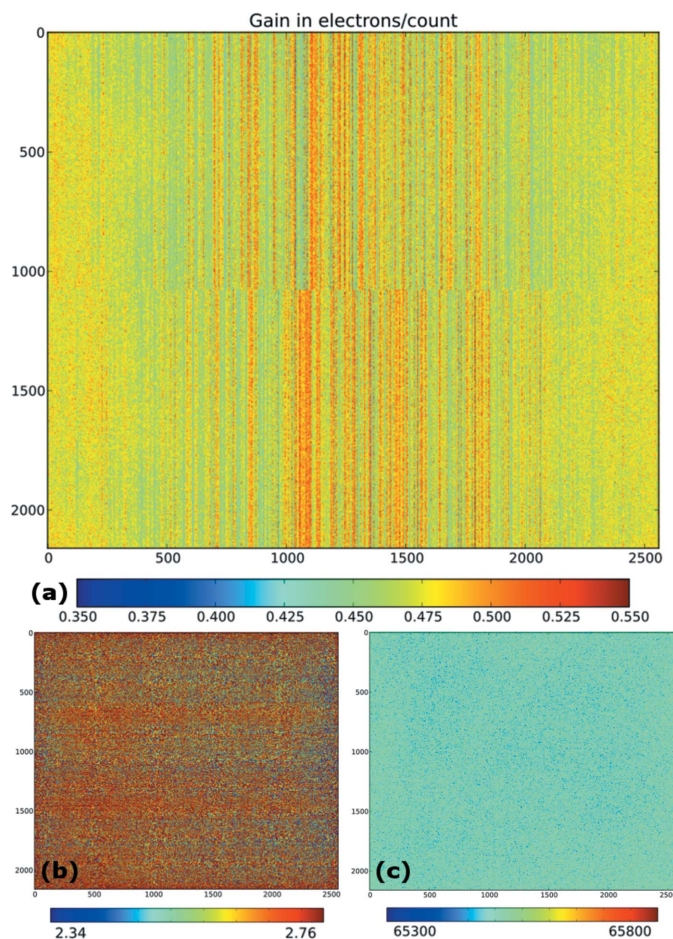


Figure 15

(a) Map of the gain of individual pixels. An average gain value of 0.473 with a standard deviation of 0.05% was calculated. (b) Map of the readout noise of individual pixels. The average readout noise was found to be 3.03 counts with a standard deviation of 0.3% . (c) Map of the full-well capacity of individual pixels. The mean full-well capacity was found to be 65503 counts with a deviation of less than 0.001% .

counts with a deviation of 0.3% . This corresponds to a readout noise of $1.43 e^-$ after applying the conversion of $0.473 e^- \text{ count}^{-1}$ obtained from the gain map. This value is even marginally below the $1.5 e^-$ specified in the PCO.Edge's data sheet. Finally, we report in Fig. 15(c) a map of the full-well capacity of the detector in digital counts. The full-well capacity is highly uniform across the whole detector. The mean full-well capacity was calculated as 65502.9 digital counts with a deviation of less than 1% . Converted digital to electrons, this means that each pixel can hold $30982.9 e^-$ on average, which is almost $1000 e^-$ more than specified by the vendor, and is reflected in a delayed saturation point.

4. Conclusions

The results reported show how the detection system based on the PCO.Edge5.5 satisfies well the daily needs of the biomedical beamline ID17. Linearity measurement shows that the detector has excellent linearity in its photo-response. The MTF of the detection system demonstrates its resolution

capabilities that allow detection of details in the $20 \mu\text{m}$ range for the $1\times$ and around $12 \mu\text{m}$ for $2\times$ lens system. The detector exhibits low noise overall in accord with the result obtained using the LED source. This results in a high DQE of the detector once the artefacts and the fixed pattern noise are removed. Of course, the real DQE would be lower as fixed pattern noise will always be present in the images since it is inherent. However, the gain map obtained through the PTC measurement proves that the fixed pattern is very low for this detector.

The relatively large field of view of the detector makes it well suited for imaging of extended biological samples and small animals. The high resolution and low noise reveal even the smallest details with high contrast due to the large full-well capacity of the detector. The low readout noise and high QE make it also a suitable option for *in vivo* imaging. The detector presents good capabilities when applied to fast imaging; high frame rates can be achieved especially if a ROI is selected, that is fundamental for *in vivo* applications. Short integration times may be slightly influenced by the lag effect of the detection system, but very likely this effect is minor compared with the natural degradation of the spatial resolution due to the continuous rotation of the sample used in the so-called 'continuous mode' of tomographic scans performed in the imaging experiments at ID17.

Acknowledgements

We would like to thank the ISSD group of the ESRF, and in particular Elia Chinchio and Paul Antoine Douissard for lending us the LED with the integrating sphere and for useful discussions and design of the coated scintillator screen, and Herwig Requardt for his support in the setup preparation.

Funding information

The following funding is acknowledged: grant K2015-99X-22731-01-4 from the Swedish Research Council to LB.

References

- Banhart, J. (2008). Editor. *Advanced Tomographic Methods in Materials Research and Engineering*, ch. 10. Oxford University Press.
- Boone, J. M. & Seibert, J. A. (1994). *Med. Phys.* **21**, 1541–1545.
- Coan, P., Peterzol, A., Fiedler, S., Ponchut, C., Labiche, J. C. & Bravin, A. (2006). *J. Synchrotron Rad.* **13**, 260–270.
- Cunningham, I. (2000). *Handbook of Medical Imaging*, Vol. 1, edited by R. L. Van Metter, J. Beutel & H. Kundel, ch. 2, pp. 79–159. Washington: SPIE.
- Denvir, D. J. & Conroy, E. (2003). *Proc. SPIE*, **4877**, 55–68.
- Dobbins, J. I. (2000). *Handbook of Medical Imaging*, Vol. 1, edited by R. L. Van Metter, J. Beutel & H. Kundel, ch. 3, pp. 161–221. Washington: SPIE.
- Escartin, T., Nano, T. F. & Cunningham, I. A. (2016). *Proc. SPIE*, **9783**, 97833W.
- Fujita, H., Tsai, D.-Y., Itoh, T., Doi, K., Morishita, J., Ueda, K. & Ohtsuka, A. (1992). *IEEE Trans. Med. Imaging*, **11**, 34–39.
- Gruner, S. M., Tate, M. W. & Eikenberry, E. F. (2002). *Rev. Sci. Instrum.* **73**, 2815–2842.

- IEC (2003). *Medical electrical equipment – Characteristics of digital X-ray imaging devices*. International Electrotechnical Commission, Geneva, Switzerland.
- Janesick, J. R. (2007). *Photon Transfer*. Bellingham: SPIE.
- Janesick, J. R., Klaasen, K. & Elliott, T. (1985). *Proc. SPIE*, **0570**, 7–19.
- Luo, T. D., Li, B. K., Yang, S. H., Guo, M. A. & Yan, M. (2016). *Nucl. Instrum. Methods Phys. Res. A*, **822**, 43–47.
- Lytaev, P., Hipp, A., Lottermoser, L., Herzen, J., Greving, I., Khokhriakov, I., Meyer-Loges, S., Plewka, J., Burmester, J., Caselle, M., Vogelgesang, M., Chilingaryan, S., Kopmann, A., Balzer, M., Schreyer, A. & Beckmann, F. (2014). *Proc. SPIE*, **9212**, 921218.
- Siewerdsen, J. H., Cunningham, I. A. & Jaffray, D. A. (2002). *Med. Phys.* **29**, 2655–2671.
- Suortti, P., Fiedler, S., Bravin, A., Brochard, T., Mattenet, M., Renier, M., Spanne, P., Thomlinson, W., Charvet, A. M., Elleaume, H., Schulze-Briese, C. & Thompson, A. C. (2000). *J. Synchrotron Rad.* **7**, 340–347.
- Zhou, Z., Gao, F., Zhao, H. & Zhang, L. (2011). *Med. Phys.* **38**, 1600–1610.